JOC The Journal of Organic Chemistry

pubs.acs.org/joc Article

N-Acetyl Side-Chain Conformation in Saccharides: Solution Models Obtained from *MA'AT* Analysis

Reagan J. Meredith, Timothy Tetrault, Mi-Kyung Yoon, Wenhui Zhang, Ian Carmichael, and Anthony S. Serianni*

Cite This: *J. Org. Chem.* 2022, 87, 8368–8379 Read Online

ACCESS | Metrics & More | Article Recommendations | Supporting Information

ABSTRACT: *MA'AT* analysis has been applied to model the conformational properties of *N*-acetyl side-chains in biologically important GlcNAc and ManNAc monosaccharides and in a βGlcNAc-(1→4)-βGlcNAc disaccharide. Density functional theory calculations were conducted to obtain parameterized equations that relate the magnitudes and signs of 10 spin-coupling constants to conformations of the C2−N2 bonds of GlcNAc and ManNAc. Six of these equations were used with experimental *J*-couplings, measured in $H_2O/^2H_2O$ and DMSO-d_6 solvents in selectively ^{13}C-labeled compounds, to model the C1−C2−N2−C1′ torsion angle (θ_1) in GlcNAc and ManNAc residues. *MA'AT* analysis gave mean values of θ_1 of 106° for αGlcNAc and ∼116° for βGlcNAc residues, with circular standard deviations (CSDs) of 21−22° in aqueous solution, in excellent agreement with those obtained by aqueous molecular dynamics (MD) simulation. Parameter space plots revealed unique *MA'AT* fits of the data, and root mean squared deviations (<0.2 Hz) were twofold smaller than those back-calculated from MD models, indicating that the *MA'AT* models better fit the experimental *J*-couplings. Context effects on both θ_1 values were found to be small in a βGlcNAc-(1→4)-βGlcNAc disaccharide. *MA'AT* analysis gave a mean value of θ_1 of 249° for αManNAc in $H_2O/^2H_2O$, with a CSD of ∼19°, with both values in good agreement with MD. *MA'AT* models of *N*-acetyl side-chains are similar to those obtained previously for *O*-acetyl side-chains (*J. Phys. Chem. B* **2017**, *121*, 66−77). Both *O*- and *N*-acetylation conformationally constrain the C−O or C−N bonds relative to the same bonds in unsubstituted compounds. The present work confirms the ability of *MA'AT* analysis to reveal relatively small changes in mean molecular torsion angles in solution and provides additional evidence of the method as an experimental tool complementary to MD simulation.

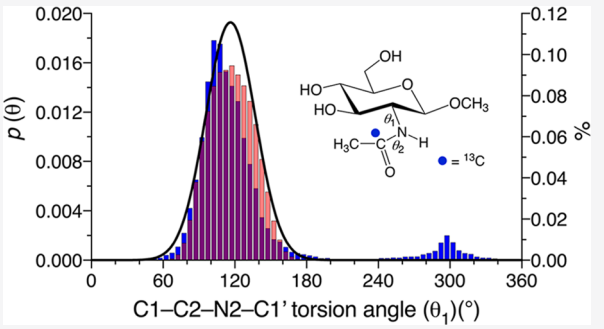

INTRODUCTION

N-Acetylation is a common side-chain modification of saccharides with potentially important implications for saccharide biological functions.[1] Aminosugars such as D-glucosamine hydrochloride (**1**) bear a positive charge in vivo that is suppressed via *N*-acetylation to give *N*-acetyl-D-glucosamine (**2**), similar to the suppression of histone positive charge via *N*-acetylation of lysine side-chains.[2] *N*-Acetylation also protects cells from the toxicity of aminosugars such as D-galactosamine.[3] Common biologically relevant monosaccharides and polysaccharides bearing *N*-acetyl side-chains include *N*-acetyl-D-glucosamine (**2**), *N*-acetyl-D-galactosamine (**3**), *N*-acetyl-neuraminate (**4**), and hyaluronate (**5**) (Scheme 1).

Two molecular torsion angles, θ_1 and θ_2, dictate the conformational properties of *N*-acetyl side-chains (Scheme 2). Recent NMR studies, assisted by selective ^{13}C-labeling, have interrogated the *cis*−*trans* equilibrium of the amide bond in *N*-acetyl (and *N*-formyl) side-chains (rotation about θ_2 in Scheme 2), and the isomerization kinetics can be measured by ^{1}H and ^{13}C saturation transfer.[4] These properties are context dependent (i.e., they are affected by the specific chemical environment, an example being *O*-glycoside linkage conformation in a disaccharide compared to that of the same linkage embedded in a larger oligosaccharide), as recently observed for *O*-acetyl side-chains,[5] leading to the expectation that they may affect receptor-binding properties and influence other structural properties of saccharides, notably those associated with *N*-glycosidic linkage conformation in N-linked glycoproteins (Scheme 3). The structure of the βGlcNAc−Asn linkage bears a close resemblance to that of the adjacent *N*-acetyl group. Thus, structural methods to evaluate the conformational properties of *N*-acetyl side-chains should be applicable to evaluating *N*-glycosidic linkage conformation.

N-acetyl side-chain conformation has been investigated in prior studies[6−9] by measuring and interpreting $^3J_{HCNH}$ values

Received: January 26, 2022
Published: June 10, 2022

https://doi.org/10.1021/acs.joc.2c00189
J. Org. Chem. 2022, 87, 8368−8379

Scheme 1. Biologically Important Monosaccharides 1−4 and a Polysaccharide 5 Bearing *N*-Acetyl Side-Chains

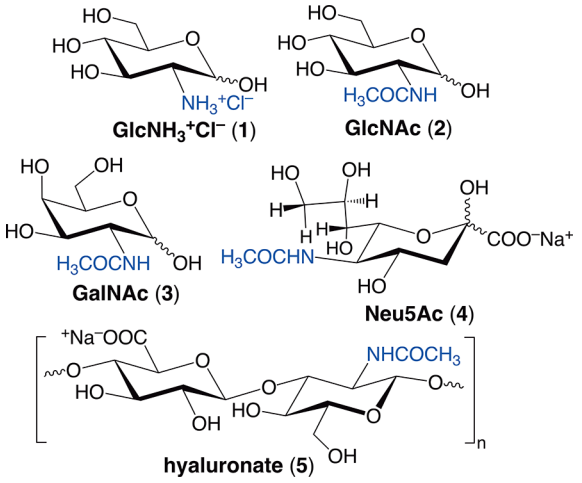

Scheme 2. Definitions of θ_1 and θ_2 in the *N*-Acetyl Side-Chain of GlcNAc Glycosides and *Cis*−*Trans* Isomerization of the Amide from the Rotation of θ_2

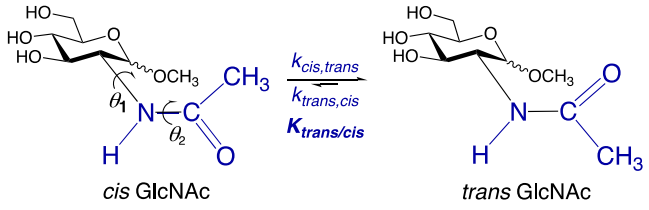

Scheme 3. Structure of βGlcNAc Appended to an Asn Side-Chain in an *N*-Linked Glycoprotein, Highlighting the Structural Similarities of the *N*-Glycosidic Linkage and the Adjacent *N*-Acetyl Side-Chain

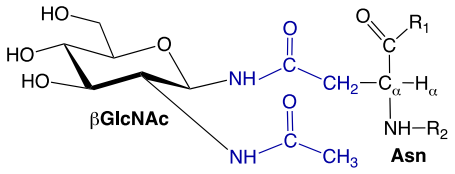

(Scheme 4) as constraints on the C−N bond (rotation about θ_1 in Schemes 2 and 4). Although this *J*-coupling is useful, it does not provide unbiased conformational assignments of θ_1. Not only is the system severely under-determined but single-point analyses cannot provide probability distribution models comparable to those obtained by molecular dynamics (MD) simulation. Prior NMR studies of βGlcNAc have shown that five additional spin-coupling constants ($^3J_{H2,C1'}$, $^3J_{C1,NH}$, $^3J_{C3,NH}$, $^3J_{C1,C1'}$, and $^3J_{C3,C1'}$; Scheme 4) are potentially useful as constraints on θ_1', giving a total of six redundant *J*-couplings to model θ_1.[9] Analogous *J*-couplings are found in peptides and proteins (Scheme S1, Supporting Information), but their structural dependencies are likely to differ from those in saccharides due to differences in coupling pathway structure.

Scheme 4. Twelve Redundant NMR Spin-Coupling Constants Sensitive to Either θ_1 or θ_2 in an *N*-Acetyl Side-Chain; Six θ_1-Sensitive *J*-Couplings (Shown in Bold) Were Used in This Work to Model θ_1

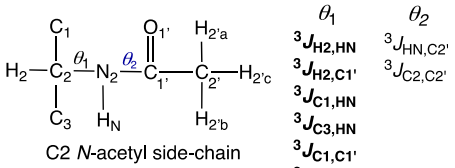

θ_1	θ_2
$^3J_{H2,HN}$	$^3J_{HN,C2'}$
$^3J_{H2,C1'}$	$^3J_{C2,C2'}$
$^3J_{C1,HN}$	
$^3J_{C3,HN}$	
$^3J_{C1,C1'}$	
$^3J_{C3,C1'}$	
$^1J_{C2,H2}$	
$^2J_{C1,C3}$	
$^2J_{C1,H2}$	
$^2J_{C3,H2}$	

The primary aim of this study was to extend the application of a new experimental method, *MA'AT* analysis (named after the Egyptian goddess, *MA'AT*), to *N*-acetyl side-chains in order to further document its ability to provide experimental conformational models comparable to those obtained by MD simulation and to test and validate the conformational models obtained by MD simulation. Parameterized *J*-coupling equations were developed for *N*-acetylated monosaccharide model structures **6**^{c}−**12**^{c} [Scheme 5; the superscript "c"

Scheme 5. In Silico Model Structures of 6^c−11^c, 12^{c}p, and 12^{c}i Used in DFT Calculations of Spin-Coupling Constants Sensitive to θ_1

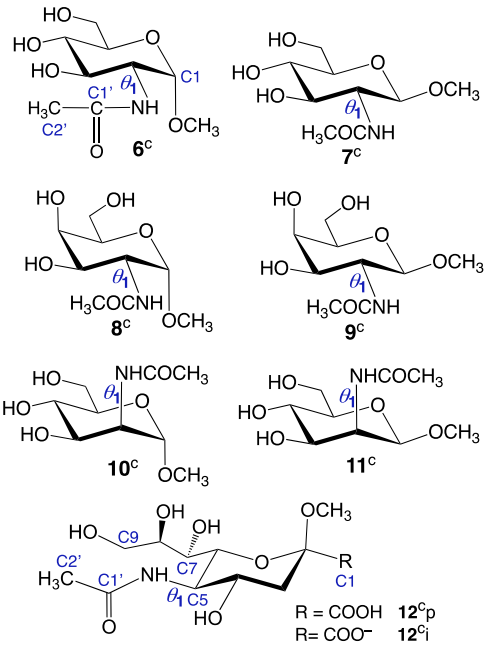

denotes in silico structures used in density functional theory (DFT) calculations] that are commonly found in biological systems. Some of these equations were then applied in *MA'AT* analyses[5,10] to generate conformational models of θ_1 in methyl 2-[1-^{13}C]acetamido-2-deoxy-α-D-glucopyranoside (**6**$^{1'}$) (the superscript denotes the ^{13}C-labeled carbonyl carbon in the side-chain), methyl 2-[1-^{13}C]acetamido-2-deoxy-β-D-glucopyranoside (**7**$^{1'}$), methyl 2-[1-^{13}C]acetamido-2-deoxy-α-D-mannopyranoside (**10**$^{1'}$), and methyl 2-[1-^{13}C]acetamido-2-deoxy-β-glucopyranosyl-(1→4)-2-[1-^{13}C]acetamido-2-deoxy-β-D-glucopyranoside (methyl β-chitobioside) (**13**$^{1'',1'''}$) (Scheme 6). The resulting *MA'AT* models of θ_1 were then compared to

https://doi.org/10.1021/acs.joc.2c00189
J. Org. Chem. 2022, 87, 8368−8379

those derived from aqueous MD simulations and to statistical data obtained on relevant crystal structures.

Scheme 6. Structures of Singly ^{13}C-Labeled $6^{1'}$, $7^{1'}$, $10^{1'}$ and $13^{1'',1'''}$ Showing Atom Numbering in the Pyranosyl Rings and Side-Chains

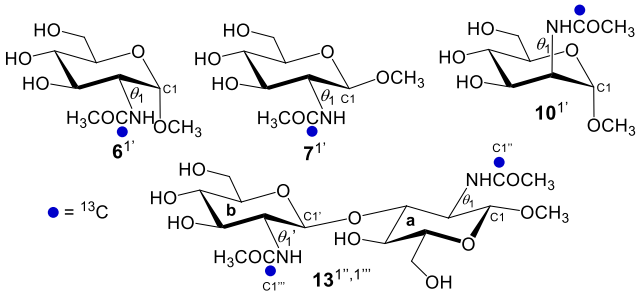

RESULTS AND DISCUSSION

Spin-Coupling Constants for *MA'AT* Analysis of θ_1 in 6^c–12^c. The ability of *MA'AT* analysis to provide models of molecular torsion angles in solution hinges on the availability of multiple, redundant spin-coupling constants that exhibit strong dependencies on the angle, and on experimental or computational methods to parameterize equations that describe these dependencies quantitatively.[5,10] This study aimed to model θ_1 in *N*-acetylated saccharides $6^{1'}$, $7^{1'}$, $10^{1'}$, and $13^{1'',1'''}$, which partly determines the disposition of the *N*-acetyl side-chain with respect to the aldohexopyranosyl ring (Scheme 2). A second torsion angle, θ_2, also affects this disposition and describes the *cis*–*trans* configuration of the amide bond (Scheme 2). Although *MA'AT* modeling of θ_2 is not treated here, prior work has described NMR methods to determine both the *cis*–*trans* equilibrium and the kinetics of *cis*–*trans* isomerization in *N*-acyl side-chains of saccharides in solution.[4]

Multiple NMR spin-couplings exist in the vicinity of the *N*-acetyl side-chain of saccharides that could be useful in *MA'AT* modeling of θ_1. Twenty *J*-couplings were investigated initially in 7^c to determine their dependencies on θ_1, and more specifically, their dynamic ranges (Figures S3–S5, Supporting Information). Spin-couplings with larger dynamic ranges (i.e., large differences between their minimal and maximal values upon 360° rotation of the torsion angle) are particularly attractive for *MA'AT* analysis due to their greater overall sensitivity to changes in the angle. It was expected that the *J*-couplings found to have desirable properties for *MA'AT* analysis of θ_1 in βGlcNAc **7** (as determined from DFT calculations on 7^c) would be equally desirable for similar analyses of θ_1 in αGlcNAc **6**, αGalNAc **8**, βGalNAc **9**, αManNAc **10**, βManNAc **11**, and αNeu5Ac **12**. DFT calculations were conducted in which θ_1 in **7** was rotated through 360° in 15° increments and the 20 *J*-values were calculated in the resulting geometry-optimized structures. The plots of these results are shown in Figures S3–S5 (see the Supporting Information). Six one-bond (^1J) spin-couplings were examined: $^1J_{C2,H2}$, $^1J_{C1,C2}$, $^1J_{C2,C3}$, $^1J_{C2,N2}$, $^1J_{N2,H}$, and $^1J_{N2,C1'}$ (Figure S3, Supporting Information). Within this group, $^1J_{C2,N2}$ and $^1J_{N2,C1'}$ are only modestly affected by θ_1, showing dynamic ranges of 1.6 and 0.7 Hz, respectively, and therefore are not very useful for *MA'AT* analysis. Intermediate dynamic ranges (3.8–4.7 Hz) were observed for $^1J_{C1,C2}$, $^1J_{C2,C3}$, and $^1J_{N2,NH}$, while $^1J_{C2,H2}$ showed the greatest sensitivity to θ_1 (11.5 Hz). However, while four ^1J values have attractive characteristics, they are affected by secondary conformational factors (e.g., effects caused by the rotation of proximal C–O bonds), complicating their use to model θ_1. It is noteworthy that, for each ^1J value investigated, the difference between the calculated coupling for θ_1 = 120° (C1′ and H2 eclipsed) and θ_1 = 300° (C1′ and H2 *anti*) is relatively small (<∼2 Hz) (Figure S3, Supporting Information), such that qualitative inspections of their magnitudes will not yield reliable information on the relative populations of the two most likely conformations of θ_1.

Eight two-bond (geminal) spin-couplings ($^2J_{C1,H2}$, $^2J_{C3,H2}$, $^2J_{H2,N2}$, $^2J_{C1,N2}$, $^2J_{C3,N2}$, $^2J_{C1,C3}$, $^2J_{C2,NH}$, and $^2J_{C2,C1'}$; Figure S4, Supporting Information) were calculated in βGlcNAc 7^c. Small dynamic ranges (0.8–1.4 Hz) were observed for $^2J_{C1,H2}$, $^2J_{H2,N2}$, $^2J_{C3,N2}$, $^2J_{C2,NH}$, and $^2J_{C2,C1'}$. Of the remaining three values, $^2J_{C3,H2}$ and $^2J_{C1,C3}$ have attractive dynamic ranges (3.0 and 4.5 Hz, respectively), particularly the latter. However, like the ^1J values, the difference between the calculated couplings for θ_1 = 120° (H2–C2–N2–H = 180°) and 300° (H2–C2–N2–H = 0°) is relatively small for most ^2J values (<∼1 Hz) (Figure S4, Supporting Information), making them somewhat less attractive to model θ_1 using *MA'AT* analysis.

Six vicinal (three-bond) spin-couplings ($^3J_{H2,NH}$, $^3J_{C1,NH}$, $^3J_{C3,NH}$, $^3J_{H2,C1'}$, $^3J_{C1,C1'}$, and $^3J_{C3,C1'}$; Figure S5, Supporting Information) were calculated in βGlcNAc 7^c. All exhibit significant dynamic ranges with respect to θ_1 (3–11 Hz), with ranges decreasing in the order $^3J_{HH} > {}^3J_{CH} > {}^3J_{CC}$, as expected.

The abovementioned results indicated that six ^3J values and one ^2J value ($^2J_{C1,C3}$) are most useful for *MA'AT* modeling of θ_1 in **7**. As discussed below, however, only the six vicinal *J*-couplings were used to model θ_1 in αGlcNAc **6**, βGlcNAc **7**, and αManNAc **10**, and θ_1 and θ_1' in disaccharide **13** in this work due to their ease and accuracy of measurement (i.e., only ^{13}C-labeling at C1′ of the *N*-acetyl side-chain was required to measure these *J*-couplings in $6^{1'}$, $7^{1'}$, $10^{1'}$, and $13^{1'',1'''}$) (Scheme 6).

Parameterization of Spin-Coupling Equations for *MA'AT* Analysis of θ_1 in 6^c–12^c. Nine spin-coupling equations ($^3J_{H2,NH}$, $^3J_{H2,C1'}$, $^3J_{C1,NH}$, $^3J_{C3,NH}$, $^3J_{C1,C1'}$, $^3J_{C3,C1'}$, $^2J_{C1,C3}$, $^2J_{C1,H2}$, and $^2J_{C3,H2}$) were parameterized for 6^c–12^c (see eqs S1–S54, Supporting Information). Plots of the calculated dependencies of these *J*-couplings on θ_1 for α/β GlcNAc (6^c/7^c) and α/β-GalNAc (8^c/9^c) (Figures 1 and 2) showed that the effect of C4 configuration on *J*-coupling behavior is small, leading to generalized equations for αGlcNAc/αGalNAc (eqs S1–S9, Supporting Information) and βGlcNAc/βGalNAc (eqs S10–S18, Supporting Information). Separate equation parameterizations were required for αManNAc 10^c (eqs S19–S27, Supporting Information), βManNAc 11^c (eqs S28–S36, Supporting Information), and for the protonated and ionized forms of αNeu5Ac (12^cp/i) (eqs S37–S54, Supporting Information).

The plots in Figure 1 show that anomeric configuration in 6^c–9^c exerts a small effect on the dependencies of $^3J_{H2,NH}$, $^3J_{C1,NH}$, $^3J_{C3,NH}$, $^3J_{H2,C1'}$, $^3J_{C1,C1'}$, and $^3J_{C3,C1'}$ on θ_1. The overall shapes of the plots for anomeric pairs are conserved but small changes in the phase and/or amplitude are observed between the α- and β-anomers. This behavior differs from that observed

https://doi.org/10.1021/acs.joc.2c00189
J. Org. Chem. 2022, 87, 8368–8379

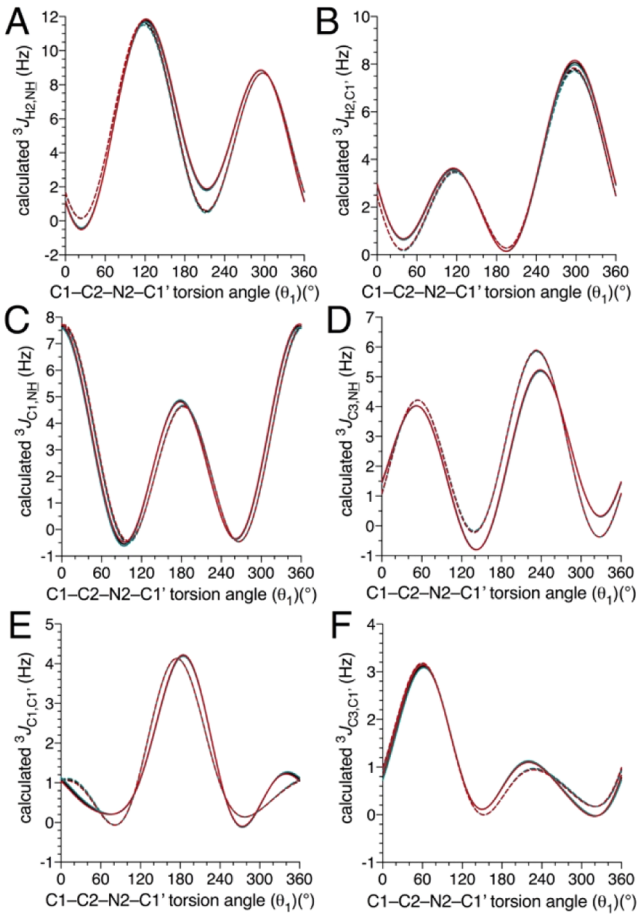

Figure 1. Calculated vicinal spin-coupling constants in αGlcNAc **6**^{c} (solid green), βGlcNAc **7**^{c} (dashed green), αGalNAc **8**^{c} (solid red), and βGalNAc **9**^{c} (dashed red) as a function of θ_1. (A) $^3J_{H2,NH}$. (B) $^3J_{H2,C1'}$. (C) $^3J_{C1,NH}$. (D) $^3J_{C3,NH}$. (E) $^3J_{C1,C1'}$. (F) $^3J_{C3,C1'}$. In each plot, the overlapping curves for **6**^{c} and **8**^{c} were combined to give the solid black curves corresponding to eqs S1–S6, and the overlapping curves for **7**^{c} and **9**^{c} were combined to give the dashed black curves corresponding to eqs S10–S15 (see the Supporting Information for the equations).

for the plots of geminal spin-couplings shown in Figure 2A–C. The effect of anomeric configuration is more pronounced for $^2J_{C1,C3}$ and $^2J_{C1,H2}$ (Figure 2A,B) than for $^2J_{C3,H2}$ (Figure 2C).[11] For $^2J_{C1,C3}$, the effect is similar to that observed in simple aldohexopyranosyl rings in which $^2J_{C1,C3}$ is strongly positive when the C1–O1 and C3–O3 bonds are both equatorial, essentially zero when one C–O bond is axial and the other equatorial, and moderately negative when both C–O bonds are axial.[12−14] $^2J_{C1,H2}$ values are expected to be more negative in β-anomers βGlcNAc **7**^{c} and βGalNAc **9**^{c} than in α-anomers αGlcNAc **6**^{c} and αGalNAc **8**^{c}, based on the behavior of $^2J_{C1,H2}$ values in simple aldohexopyranosyl rings bearing equatorial C2–O2 bonds.[11] For example, $^2J_{C1,H2}$ is +1.0 Hz in methyl α-D-glucopyranoside and −6.3 Hz in methyl β-D-glucopyranoside.[15] However, in general, calculated $^2J_{C1,H2}$ values in **6**^{c}–**9**^{c} appear to shift to more negative values due to the substitution of a C2–O2 bond with a C2–N2 bond, consistent with observations made previously.[8]

Plots similar to those shown in Figures 1 and 2 were also generated for **10**^{c}–**12**^{c}p/i (Figures S1, S2, S7, and S8), from which corresponding parameterized eqs S19–S54 were obtained (see the Supporting Information).

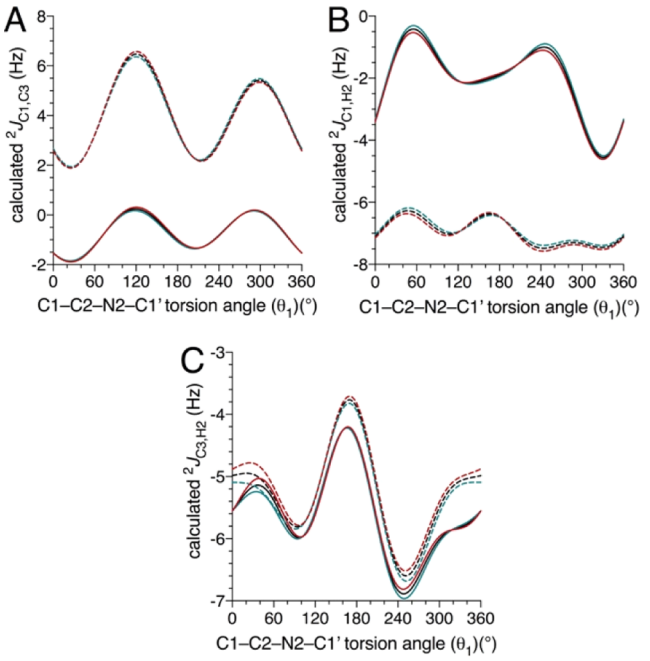

Figure 2. Calculated geminal spin-coupling constants in αGlcNAc **6**^{c} (solid green), βGlcNAc **7**^{c} (dashed green), αGalNAc **8**^{c} (solid red), and βGalNAc **9**^{c} (dashed red) as a function of θ_1. (A) $^2J_{C1,C3}$. (B) $^2J_{C1,H2}$. (C) $^2J_{C3,H2}$. In each plot, the overlapping curves for **6**^{c} and **8**^{c} were combined to give the solid black curves corresponding to eqs S7–S9, and the overlapping curves for **7**^{c} and **9**^{c} were combined to give the dashed black curves corresponding to eqs S16–S18 (see the Supporting Information for the equations).

***MA'AT* Modeling of θ_1 in Monosaccharides 6$^{1'}$, 7$^{1'}$, and 10$^{1'}$.** Selective ^{13}C-labeling at C1′ in **6**$^{1'}$, **7**$^{1'}$, and **10**$^{1'}$ allowed experimental measurements of $^3J_{H2,NH}$, $^3J_{C1,NH}$, $^3J_{C3,NH}$, $^3J_{H2,C1'}$, $^3J_{C1,C1'}$, and $^3J_{C3,C1'}$ in aqueous solution and DMSO-d_6 for each compound (Table 1). The experimental *J*-couplings and corresponding DFT-parameterized eqs S1–S27 (Support-

Table 1. J_{HH}, J_{CH}, and J_{CC} Values[a] in αGlcNAcOCH$_3$ (6$^{1'}$), βGlcNAcOCH$_3$(7$^{1'}$), and αManNAcOCH$_3$ (10$^{1'}$) in Aqueous Solution and DMSO-d_6

	aqueous solution			DMSO-d_6		
	compound			compound		
J-coupling	**6**$^{1'}$	**7**$^{1'}$	**10**$^{1'}$	**6**$^{1'}$	**7**$^{1'}$	**10**$^{1'}$
$^3J_{H2,NH}$	9.7	10.1	11.1	8.3	9.1	8.0
$^3J_{C1,NH}$	0.6	0.7	1.1	0.5	0.7	1.1
$^3J_{C3,NH}$	1.3	1.0	1.3	1.4	1.0	1.0
$^3J_{H2,C1'}$	3.4	3.5	3.3	nm	3.8	br
$^3J_{C1,C1'}$	1.0	1.4	1.4	0.7	1.2	br
$^3J_{C3,C1'}$	1.5	1.2	1.0	1.8	0.9	1.3

[a]In Hz at ∼25 °C, ±0.1 Hz. $^3J_{H2,NH}$ and $^3J_{H2,C1'}$ values were measured from 1D ^{1}H NMR spectra. $^3J_{C1,C1'}$ and $^3J_{C3,C1'}$ values were measured from 1D ^{13}C{^{1}H} NMR spectra. $^3J_{C1,NH}$ and $^3J_{C3,NH}$ values were measured from 2D HSQC-HECADE spectra. For the *J*-couplings measured in aqueous solution, *J*-values not involving the NH hydrogen were measured in ^2H_2O and the remaining three *J*-couplings were measured in 93/7 *v*/*v* $H_2O/^2H_2O$. All ^3J-couplings have positive signs. A "nm" entry denotes a *J*-value that could not be measured accurately. A "br" entry denotes a non-zero *J*-value that is <0.7 Hz (broadened signal).

https://doi.org/10.1021/acs.joc.2c00189
J. Org. Chem. 2022, 87, 8368−8379

ing Information) were then used as inputs in *MA'AT* analyses of θ_1. Multiple *MA'AT* models were obtained for θ_1 in αGlcNAc **6**$^{1'}$, βGlcNAc **7**$^{1'}$, and αManNAc **10**$^{1'}$ using different combinations of the six spin-coupling constants measured in either aqueous solution or DMSO-d_6 (Tables S1−S12, Figure S9, Supporting Information) to determine how the models are affected by the ensemble of *J*-couplings used in the analysis. The *MA'AT* models obtained from these fits gave parameter space plots indicative of unique solutions (for representative parameter space plots, see Figure S16, Supporting Information) in nearly all the cases. The multiple models were combined to obtain an average model of θ_1 in **6**$^{1'}$, **7**$^{1'}$, and **10**$^{1'}$, and the average *MA'AT* models were superimposed on those obtained from aqueous MD simulations (1 μs). The results are shown in Figure 3, and the statistics obtained from the data fitting are summarized in Table 2.

For αGlcNAc **6** in aqueous solution, *MA'AT* analyses gave an average mean θ_1 of 106.3 ± 2.5° and an average circular standard deviation (CSD) of 22.1 ± 4.0°. These results compare favorably with those obtained by aqueous MD simulation, which gave respective values of 104.2 and 25.1°. The quality of the *MA'AT* fit is reflected in the average root-mean-squared deviation (RMSD) of 0.15 ± 0.07 Hz, which is smaller than 0.27 Hz obtained from MD, indicating a slightly better fit to the experimental data. For βGlcNAc **7**, *MA'AT* analysis gave an average mean value of θ_1 of 116.3 ± 1.8° and an average CSD of 20.7 ± 4.5°. These results closely mimic those obtained by MD, the latter giving respective values of 117.0° and 18.6°. As found for **6**, the RMSD obtained from the *MA'AT* model of **7** (0.17 ± 0.11 Hz) is slightly smaller than that obtained from the MD model. For αManNAc **10**, an average mean value of θ_1 of 249.0 ± 1.2° and an average CSD of 18.9 ± 1.4° were obtained from *MA'AT* analysis. These results resemble those obtained by MD, the latter giving a mean value of 251.0° and a CSD of 24.3°. In this case, the RMSD from the *MA'AT* model (0.08 ± 0.02) was significantly smaller than that calculated from the MD model (0.84 Hz), indicating that the former model fits the experimental data better. Overall, *MA'AT* analysis of θ_1 in **6**, **7**, and **10** recapitulates the MD data well in terms of both mean values of θ_1 and the degree of librational motion about the mean values. The latter motion, embodied in the CSDs, ranges from 19 to 22°, comparable to the 19−25° range determined by MD. The *N*-acetyl side-chain highly prefers a conformation in **6**, **7**, and **10** where the C2−H2 bond in the aldohexopyranosyl ring is nearly eclipsed with the C1′═O bond of the side-chain (the *anti*-geometry in which H2 is *anti* to the NH hydrogen) (Scheme 7).

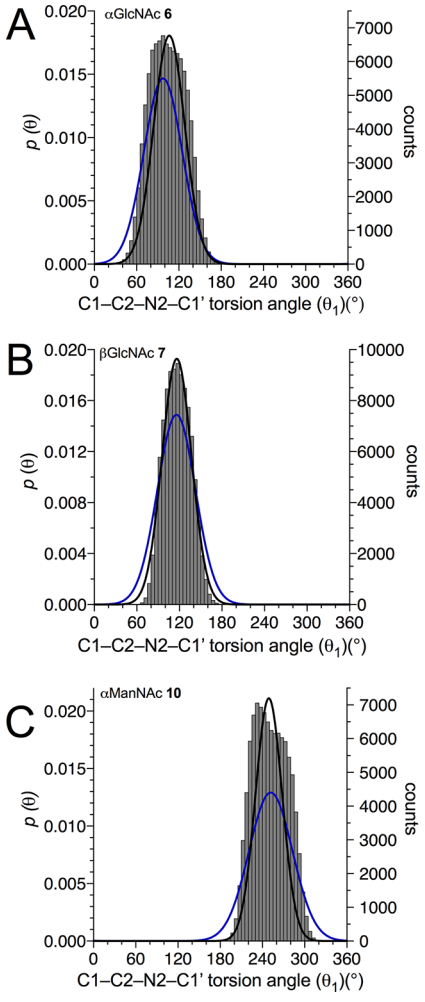

Figure 3. Average *MA'AT* models of θ_1 in αGlcNAc **6** (A), βGlcNAc **7** (B), and αManNAc **10** (C) in aqueous solution (black curves) and in DMSO-d_6 (blue curves) superimposed on models obtained by aqueous MD simulation (1 μs) (gray envelopes). The fitting statistics are summarized in Table 2, and representative parameter space plots are shown in Figure S16 of the Supporting Information.

The solution behavior of θ_1 in αGlcNAc **6**, βGlcNAc **7**, and αManNAc **10** determined by *MA'AT* analysis was compared to that observed in crystal structures containing *N*-acetylated sugar residues (Tables S13, S14, and Figures S10, S11, Supporting Information). Because GlcNAc residues significantly outnumber other types of *N*-acetylated sugars in the Protein Data Bank (PDB), only PDB data for these residues are plotted against models of θ_1 determined by *MA'AT* and MD (Figure 4). In general, there is very good overlap of the population distributions of θ_1 determined by the three methods (see statistics in Table 2), with the *anti*-geometry highly preferred (θ_1 near 120°), although the PDB contains a minor conformation with θ_1 near 300°, that is, in a geometry where the C2−H2 and N2−H bonds are eclipsed (*syn* geometry). The structures containing these aberrant conformations mostly involve complexes with proteins where the binding interaction stabilizes the otherwise less preferred *syn* form. This behavior is discussed in more detail below.

The experimental *J*-couplings measured in αGlcNAc **6**$^{1'}$, βGlcNAc **7**$^{1'}$, and αManNAc **10**$^{1'}$ (Table 1) are essentially the same in aqueous solution and DMSO-d_6, the exception being $^3J_{H2,NH}$, which is consistently smaller in DMSO-d_6 by 1−3 Hz. *MA'AT* modeling of θ_1 in DMSO-d_6 gave similar but not identical mean values of θ_1 to those found in aqueous solution (Figure 3, Table 2). The effect of the solvent on the mean value of θ_1 was discernible for **6**, whereas the effect is negligible for **7** (Figure 5). The CSDs in DMSO-d_6 are slightly larger than those in the aqueous solution, especially for **10**, indicating greater librational motion in nonaqueous solvent, but more data are needed to confirm this behavior.

***MA'AT* Modeling of θ_1 and θ_1' in Disaccharide 13.** *N*-Acetyl side-chain conformations in methyl β-chitobioside **13**$^{1'',1'''}$ were determined to demonstrate the application of *MA'AT* analysis to structures more complex than mono-

https://doi.org/10.1021/acs.joc.2c00189
J. Org. Chem. 2022, 87, 8368−8379

Table 2. Statistics from *MA'AT* Modeling of θ_1 in αGlcNAcOCH$_3$ (6), βGlcNAcOCH$_3$ (7), and αManNAcOCH$_3$ (10) in Aqueous Solution and DMSO-d_6

	mean (deg)	std. error (deg)	CSD[d] (deg)	std. error (deg)	RMSD[e] (Hz)
			αGlcNAcOCH$_3$ (**6**)		
average[a] (aqueous)	106.3 ± 2.5	8.3 ± 1.8	22.1 ± 4.0	10.4 ± 8.2	0.15 ± 0.07
average[a] (DMSO-d_6)	97.5 ± 2.6	8.1 ± 2.7	27.2 ± 3.2	10.2 ± 6.6	0.10 ± 0.06
MD[b]	104.2		25.1		0.27
X-ray[c]	113.7		45.7		0.49
			βGlcNAcOCH$_3$ (**7**)		
average (aqueous)	116.3 ± 1.8	10.4 ± 2.0	20.7 ± 4.5	10.1 ± 7.7	0.17 ± 0.11
average (DMSO-d_6)	115.8 ± 4.2	12.5 ± 3.4	26.8 ± 5.2	7.6 ± 2.9	0.39 ± 0.20
MD	117.0		18.6		0.29
X-ray	112.2		35.6		0.22
			αManNAcOCH$_3$ (**10**)		
average (aqueous)	249.0 ± 1.2	8.2 ± 2.2	18.9 ± 1.4	9.4 ± 3.7	0.08 ± 0.02
average (DMSO-d_6)	251.7 ± 5.6	9.8 ± 3.3	30.9 ± 4.7	7.6 ± 2.3	0.18 ± 0.10
MD	251.0		24.3		0.38
X-ray	238.5		14.6		0.55

[a]Average ±1 standard deviation obtained from *MA'AT* models of θ_1 obtained using different combinations of redundant *J*-couplings (see Tables S1, S3, S5, S7, S9, and S11 for aqueous, and Tables S2, S4, S6, S8, S10, and S12 for DMSO-d_6, in the Supporting Information). [b]Values obtained from 1-μs aqueous MD simulations. [c]Values obtained from X-ray database analyses. [d]CSD = circular standard deviation. [e]RMSD = root mean squared deviation.

Scheme 7. Mean θ_1 Torsion Angles in 6, 7, and 10 in $H_2O/^2H_2O$ Determined from *MA'AT* Analysis, Showing near Eclipsing of the C2−H2 and C1′═O Bonds

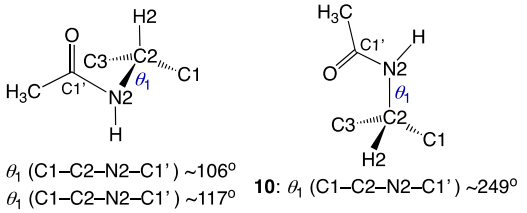

6: θ_1 (C1–C2–N2–C1′) ~106°
7: θ_1 (C1–C2–N2–C1′) ~117°
10: θ_1 (C1–C2–N2–C1′) ~249°

saccharides and to investigate the effect of structural context on conformation. Experimental *J*-couplings sensitive to θ_1 in residue a and θ_1' in residue b were measured in aqueous solution and DMSO-d_6 (Table 3, Supporting Information) (see Scheme 6 for residue assignments). Different combinations of these *J*-couplings were then used in *MA'AT* analyses (Tables S18−S25, Supporting Information), which gave multiple models that were used to calculate average models of θ_1 and θ_1' (Table 4 and Figures 6 and S15). In aqueous solution, the average mean value of θ_1 (114.6 ± 1.5°) and its CSD (22.3 ± 3.3°) are similar to those found for βGlcNAc **7**

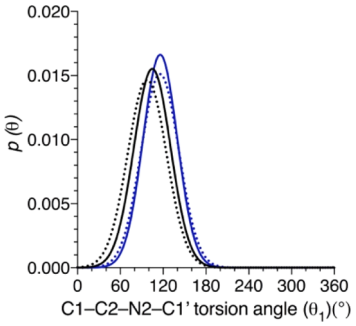

Figure 5. Effect of solvent on *MA'AT* models of θ_1 in αGlcNAc **6** and βGlcNAc **7**. Black: **6**, aqueous solution. Black dotted: **6**, DMSO-d_6. Blue: **7**, aqueous solution. Blue dotted: **7**, DMSO-d_6.

(116.3 ± 1.8 and 20.7 ± 4.5°, respectively; Table 2). Both side-chains are located on a terminal βGlcNAc residue, and potential context effects are likely to be small. On the other hand, the average mean value of θ_1' (110.0 ± 1.6°) in disaccharide **13** is smaller than that of θ_1 in **7** and **13**, suggesting that the "internal" *N*-acetyl side-chain may experience local effects that influence its geometry in solution. This behavior is also observed in the values of θ_1 and θ_1' in **13**

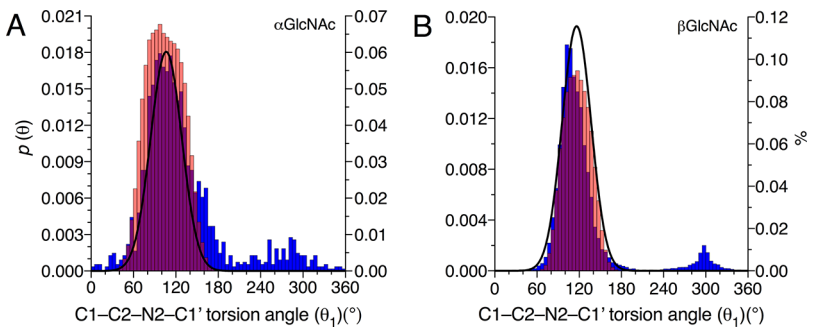

Figure 4. Solution models of θ_1 in αGlcNAcOCH$_3$ (**6**) (A) and βGlcNAcOCH$_3$ (**7**) (B) determined by *MA'AT* analysis in $H_2O/^2H_2O$ (bold blue curves) superimposed on corresponding models determined by MD (hatched yellow) and from crystal structures found in the PDB (hatched blue). The area in red is occupied by all three models.

https://doi.org/10.1021/acs.joc.2c00189
J. Org. Chem. 2022, 87, 8368−8379

Table 3. J_{HH}, J_{CH}, and J_{CC} Values[a] in βGlcNAc-(1→4)-βGlcNAcOCH$_3$ ($13^{1'',1'''}$) in Aqueous Solution and DMSO-d_6

	aqueous solution		DMSO-d_6	
J-coupling	residue a	residue b	residue a	residue b
$^3J_{H2,NH}$	9.9	10.2	9.0	9.3
$^3J_{C1,NH}$	0.7	0.6	0.6	0.5
$^3J_{C3,NH}$	1.0	1.3	0.9	0.8
$^3J_{H2,C1'}$	3.3	3.4	nm	nm
$^3J_{C1,C1'}$	1.1	1.0	1.0	0.9
$^3J_{C3,C1'}$	1.1	1.3	1.0	1.2

[a]In Hz at ∼25 °C, ±0.1 Hz. Residue a: βGlcNAc-(1→4)-βGlcNAcOCH$_3$. Residue b: βGlcNAc-(1→4)-βGlcNAcOCH$_3$. $^3J_{H2,NH}$ and $^3J_{H2,C1'}$ values were measured from 1D ^{1}H NMR spectra. $^3J_{C1,C1'}$ and $^3J_{C3,C1'}$ values were measured from 1D $^{13}C\{^1H\}$ NMR spectra. $^3J_{C1,NH}$ values were measured from 2D HSQC-HECADE spectra. For J-couplings measured in aqueous solution, J-values not involving the NH hydrogen were measured in ^2H_2O and the remaining three J-couplings measured in 93/7 v/v $H_2O/^2H_2O$. All J-couplings have positive signs. A "nm" entry denotes a J-value that could not be measured accurately.

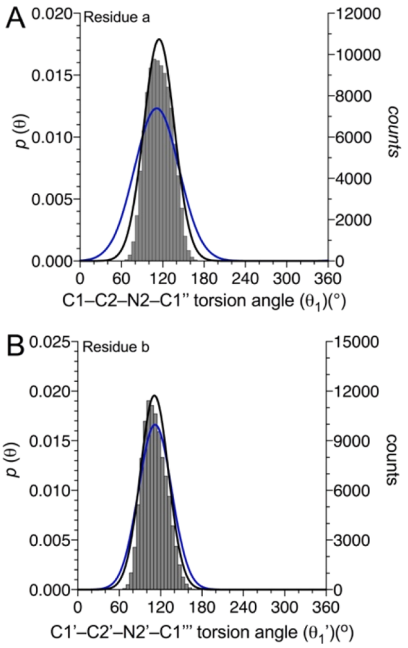

Figure 6. Average *MA'AT* models of θ_1 in residue a (A) and θ_1' in residue b of disaccharide **13** in aqueous solution (black curves) and in DMSO-d_6 (blue curves) superimposed on models obtained by aqueous MD simulation (1-μs) (gray envelopes). The fitting statistics are summarized in Table 4, and representative parameter space plots are shown in Figure S16 of the Supporting Information.

determined by aqueous MD simulation (Table 4). This difference is smaller in DMSO-d_6 and may not be statistically significant (Table 4). The trends in the mean values of θ determined by MD and *MA'AT* analysis in aqueous solutions are conserved, namely, θ_1 (**7**) > θ_1 (**13**) > θ_1' (**13**) > θ_1 (**6**).

The CSDs in DMSO-d_6 for both θ_1 and θ_1' determined from *MA'AT* analysis are larger than those found in aqueous solutions, consistent with observations made in αGlcNAc **6**, βGlcNAc **7**, and αManNAc **10** (Table 2) and indicating greater librational motion in nonaqueous solvent. *MA'AT* analysis indicates greater flexibility in both θ_1 and θ_1' in disaccharide **13** than predicted by MD simulation, a result that differs from those obtained on **6** and **7**. Additional studies will be needed to establish whether the larger CSDs for θ_1 and θ_1' in **13** obtained by *MA'AT* analyses, compared to those obtained by MD, are generally observed in *N*-acetyl side-chains of di- and oligosaccharides, and whether adjustments in the GLYCAM force field are warranted.

CONCLUSIONS

The aim of this study was to apply a newly developed experimental NMR method, *MA'AT* analysis,[10] to investigate the solution conformations of *N*-acetyl side-chains in saccharides. This work extends prior studies of 2-*N*-acetylated aldohexopyranosyl rings in which ensembles of spin-couplings (J_{HH}, J_{CH}, J_{CC}, J_{NH}, and J_{NC}) in the rings and side-chains,[8] parameterized equations sensitive to θ_1 and amide bond configuration (*cis* and *trans*),[9] and the thermodynamics and kinetics of *cis*−*trans* isomerization of *N*-acetyl and *N*-formyl side-chains[4] were investigated. The present work also builds on recent studies in which the solution conformations of 2-*O*-acetyl side-chains in 2-*O*-acetyl-α-D-glucopyranose (**14α**) and 2-*O*-acetyl-β-D-glucopyranose (**14β**) (Scheme 8) were found to be affected by anomeric configuration, similar to findings reported here for the structurally related 2-*N*-acetyl side-chains in αGlcNAc **6** and βGlcNAc **7**.[5] The mean values of the H2−C2−O2−C1′ torsion angle γ in **14α** and **14β** were found to be −22.5 and −1.1°, respectively, with CSDs of 30 and 25°, respectively (Scheme 8). RMSDs determined from unique fits of the data were ∼0.2 Hz, which is similar to the ∼0.2 Hz RMSDs determined from *MA'AT* modeling of θ_1 in the 2-*N*-acetyl side-chains in **6** and **7**. The ∼20° difference in γ observed between **14α** and **14β** is comparable to the ∼10° difference in θ_1 between **6** and **7**. In both sets of compounds, α-anomers show less eclipsing of the C2−H2 and C═O bonds

Table 4. *MA'AT* Analysis[a] of θ_1 and θ_1' in βGlcNAc-(1→4)-βGlcNAcOCH$_3$ (13): Modeling Results and Statistics in Aqueous Solution and DMSO-d_6

residue	mean (deg)	std. error (deg)	CSD[e] (deg)	std. error (deg)	RMSD[f] (Hz)
residue a[b] (aqueous)	114.6 ± 1.5	11.0 ± 2.6	22.3 ± 3.3	8.8 ± 4.8	0.14 ± 0.07
residue a (DMSO-d_6)	113.4 ± 5.6	11.8 ± 2.5	28.0 ± 4.5	7.1 ± 2.7	0.25 ± 0.12
MD[d]	114.8		17.8		0.33
residue b[c] (aqueous)	110.0 ± 1.6	9.5 ± 2.3	20.4 ± 3.4	9.2 ± 7.3	0.14 ± 0.08
residue a (DMSO-d_6)	112.0 ± 4.5	10.5 ± 2.5	24.0 ± 5.9	9.7 ± 8.6	0.22 ± 0.11
MD	111.3		16.8		0.27

[a]All entries are average values ±1 standard deviation from *MA'AT* models of θ_1 and θ_1' obtained using different combinations of redundant J-couplings (see Tables S18−S25, Supporting Information). [b]Residue a: βGlcNAc-(1→4)-βGlcNAcOCH$_3$. [c]Residue b: βGlcNAc-(1→4)-βGlcNAcOCH$_3$. [d]Values obtained from 1-μs aqueous MD simulations. [e]CSD = circular standard deviation. [f]RMSD = root mean squared deviation.

https://doi.org/10.1021/acs.joc.2c00189
J. Org. Chem. 2022, 87, 8368−8379

Scheme 8. (A) Structures of 2-*O*-Acetyl-α,β-D-glucopyranoses (14α/β) and Identification of the Rotatable Exocyclic C2−O2 Bond, γ.(B) Mean Values of γ (Defined as the H2−C2−02−C1′ Torsion Angle) in 14α and 14β in Aqueous Solution Determined by *MA′AT* Analysis (See Ref 5)

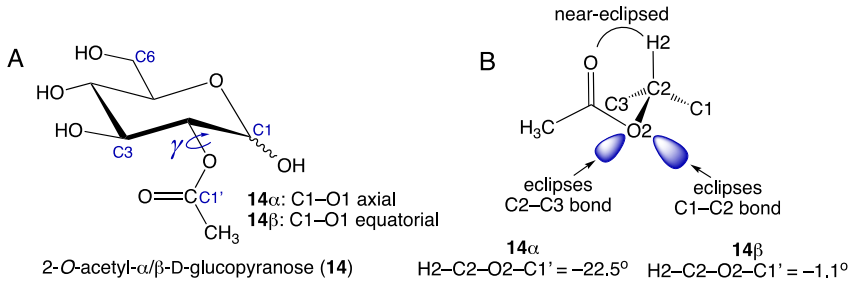

(C1−C2−O2/N2−C1′ torsion angles of ∼100°) compared to β-anomers (C1−C2−O2/N2−C1′ torsion angles of ∼116°).

Previous qualitative analyses of spin-coupling ensembles sensitive to θ_1 in βGlcNAc **7** conducted prior to the development of *MA′AT* led to models in which θ_1 values of either ∼120° (C2−H2 and C═O bonds eclipsed) or ∼300° (C2−H2 and N−H bonds eclipsed) were considered possible, with the latter more likely to be preferred. *MA′AT* analysis resolves this ambiguity by providing probability distributions of torsion angles in solution for axial (αManNAc **10**) and equatorial (αGlcNAc **6**, βGlcNAc **7**, and disaccharide **13**) C2−N2 bonds, and is sufficiently quantitative to enable investigations of context effects. Mean values of θ_1, while similar, are not identical in **6** and **7**. In **7** and in residue a of **13**, mean geometries about θ_1 are observed (∼115°) in which the C2−H2 and C═O bonds are nearly eclipsed. In αGlcNAc **6**, however, the mean value of θ_1 differs by ∼10° from that found in βGlcNAc **7** and residue a of disaccharide **13**, adopting a value near 106°. A weak 1,3-diaxial interaction between the axial O1 and the pseudoaxial NH hydrogen on the *N*-acetyl side-chain in the α-anomer may induce θ_1 to adopt a smaller value, thereby reducing the interaction (O1 and the NH hydrogen are further apart) while maintaining a geometry in which the C═O bond is nearly eclipsed by the C2−H2 bond. A weak hydrogen-bonding interaction between the NH hydrogen and a lone-pair orbital on O3 may also induce and/or stabilize the 10° shift in αGlcNAc **6**.

The effects of anomeric configuration on θ_1 observed in **6**, **7**, and **13** closely match those predicted by MD simulation, providing valuable experimental evidence supporting the MD models. Although the corresponding θ_1-sensitive spin-couplings used to model θ_1 in **6** and **7** appear to be very similar qualitatively, they differ sufficiently such that, when treated collectively, *MA′AT* analysis is capable of detecting a difference in the mean values of θ_1. These results demonstrate the ability of *MA′AT* analysis to detect both small and large context effects on conformational elements in saccharides and presumably in other types of molecules.

The *MA′AT* studies of *N*- and *O*-acetyl side-chains show that the C−N and C−O bonds of these side-chains are highly rotationally constrained compared to the same C−N and C−O bonds in the absence of acylation. An entropic cost is paid upon saccharide *N*- and *O*-acetylation, with both modifications producing more conformationally constrained products. The solution models of C2−O2 bond conformation in methyl α- and β-D-glucopyranosides are expected to differ significantly from those in **14α** and **14β**. Likewise, the solution models of the C2−N2 bond conformation in α- and β-D-glucosamines **1** and their glycosides are expected to differ significantly from those in αGlcNAc **6** and βGlcNAc **7**. The latter models, in each case, are essentially constrained to a single torsion angle with a small amount of deviation, whereas the former are likely to sample conformations over the 360° rotational itinerary, albeit staggered states are expected to predominate. In **1**, this sampling is meaningless structurally because the three states are equivalent. The solution models of free C−O bonds in a solution, determined experimentally, are currently lacking, although prior experimental data have been interpreted using conventional three-state staggered models that may not mimic behavior in solution. MD simulation has been used to support these staggered models, although current force fields are not sufficiently parameterized to allow reliable predictions of these behaviors. Current work in this laboratory aims to apply *MA′AT* modeling to this problem.

The *MA′AT* models of θ_1 for αGlcNAc **6**, βGlcNAc **7**, αManNAc **10**, and disaccharide **13** show uniformity with respect to the preferred relative orientation of the C2−H2 and side-chain amide C═O bonds. This preference may pertain to free saccharides but not to saccharides bound to proteins. For example, in crystal structures of the lectin, LecB, from *Pseudomonas aeruginosa* complexed with the Le^x tetrasaccharide, an unusual conformation has been observed in the *N*-acetyl groups of all Le^x molecules in the asymmetric unit. In these structures, the H2−C2−N2−H torsion angle adopts a *syn* conformation (torsion angles of −1.8 to −13.3°), while the H−N2−C1′−O1′ torsion angle remains in an *anti*-conformation (torsion angles of 149.7−177.1°).[16] This unusual conformation orients the acetyl group away from the protein surface, with the NH moiety pointing toward an Asp residue to allow either a direct hydrogen bond or one bridged by water. Theoretical calculations indicate that this conformation, which is unstable in solution, is stabilized by the lectin. A PDB-wide search revealed that this conformation about θ_1, is rare, occurring in ∼2% of protein-carbohydrate complexes.

The *MA′AT* modeling of θ_1 was performed with the assumption that the amide *cis*−*trans* equilibrium of the *N*-acetyl side-chain in structures such as **6**, **7**, **10**, and **13** highly favors the *trans* configuration (θ_2; C2 *anti* to C2′) (Scheme 2). This assumption is supported by prior work showing that, at 42−75 °C, $K_{trans/cis}$ for *N*-acetyl side-chains ranges from 31 to 72.[4] The equilibrium depends on the structure of the R-group attached to the carbonyl carbon. For example, *N*-formyl side-chains give $K_{trans/cis}$ of 2.5−4.2 over a similar temperature range.[4] Kinetic studies of *cis*−*trans* isomerization of 2-*N*-acetyl side-chains gave $k_{trans\rightarrow cis}$ and $k_{cis\rightarrow trans}$ of 0.02−2.6 and 1.7−80 s^{-1}, respectively, at 42−75 °C.[4] The activation barrier is expected to be influenced by solvent polarity, such that when the amide hydrogen and/or carbonyl oxygen are involved in

https://doi.org/10.1021/acs.joc.2c00189
J. Org. Chem. 2022, 87, 8368−8379

hydrogen bonding with a polar solvent (e.g., water) as a donor and/or acceptor, respectively, the barrier increases, presumably because the amide bond has greater double-bond character compared to that in non-hydrogen-bonding solvents or nonpolar environments.[17,18] Structural factors that affect θ_2 and θ_1 (Scheme 2) determine the behavior of GlcNAc and related residues in *N*-linked glycoproteins not only with respect to their *N*-acetyl side-chains but also to the structurally related *N*-linkage to the Asn side-chain of the protein (see Scheme 3).

Although variability in the fitting statistics was observed when different combinations of vicinal spin-couplings were used in *MA'AT* modeling of θ_1 in **6**, **7**, **10**, and **13**, the differences are small. The models of θ_1 predicted from *MA'AT* analysis are relatively insensitive to the particular ensemble of spin-couplings used, provided that the number used is sufficient to justify the fit. In the present work, reliable fits of the data were obtained for θ_1 even when only four of the six available vicinal spin-couplings were used in the analysis, as determined from consistently small RMSDs and from parameter space plots demonstrating unique fits of the experimental data. Nevertheless, as discussed elsewhere,[5,10] *MA'AT* models are more reliable when the number of redundant spin-couplings used is maximized, and ongoing efforts in this laboratory aim to expand ensembles of redundant *J*-couplings to include not only ^3J values but also ^1J and ^2J values, provided that the latter can be parameterized reliably and known secondary effects are accounted for (see Spin-Coupling Constants for *MA'AT* Analysis of θ_1 in **6**^{c}−**12**^{c} in Results and Discussion).

This work extends the application of *MA'AT* analysis to another conformational element of saccharides that adopts a single-state model (or largely so) in solution. However, not all conformational elements in saccharides are expected to adopt single-state models. Exocyclic hydroxyl and hydroxymethyl group conformations, and furanosyl and pyranosyl ring pseudorotation, are examples of conformational elements where multistate models likely pertain. Work is underway to apply *MA'AT* analysis to these elements.

EXPERIMENTAL SECTION

Preparation of ^{13}C-Labeled Methyl Glycosides 6$^{1'}$, 7$^{1'}$, 10$^{1'}$, and 13$^{1'',1'''}$. Methyl glycosides **6**$^{1'}$ and **7**$^{1'}$ were prepared and purified as described previously[4,8] with minor modifications. Chemical protocols to prepare **6**$^{1'}$, **7**$^{1'}$, **10**$^{1'}$, and **13**$^{1'',1'''}$ are described in the Supporting Information.

NMR Spectroscopy. High-resolution ^{1}H and ^{13}C{^{1}H} NMR spectra of ^{13}C-labeled **6**$^{1'}$, **7**$^{1'}$, **10**$^{1'}$, and **13**$^{1'',1'''}$ and their unlabeled forms were obtained on ∼20 and ∼100 m*M* aqueous (^2H_2O or 93/7 *v*/*v* $H_2O/^2H_2O$) solutions, respectively, or on ∼10 and ∼50 mM DMSO-d_6 solutions, respectively, at ∼25 °C. Sample solutions were analyzed in 5-mm NMR tubes on a 600-MHz Fourier transform NMR (FT-NMR) spectrometer equipped with a 5-mm ^{1}H−^{19}F/^{15}N−^{31}P AutoX dual broadband probe or on an 800-MHz FT-NMR spectrometer equipped with a 5 mm cryoprobe. One-dimensional (1D) ^{1}H NMR spectra were collected with ∼4 s recycle times, ∼256 K data points, and ∼6000 Hz spectral widths, and FIDs (free induction decay) were zero-filled twice to give final digital resolutions of <0.01 Hz/pt. ^{13}C{^{1}H} NMR spectra (150 MHz) were collected with ∼12,800 Hz spectral widths, ∼256 K data points, and ∼5 s recycle times, and FIDs were zero-filled twice to give final digital resolutions of <0.05 Hz/pt. FIDs were processed with resolution enhancement (Gaussian or sine-bell functions) to improve resolution and facilitate the measurement of small *J*-couplings (≥0.5 Hz), and experimental *J*-couplings were obtained with ±0.1 Hz errors unless otherwise stated. Representative NMR spectra of **6**$^{1'}$, **7**$^{1'}$, **10**$^{1'}$, and **13**$^{1'',1'''}$ and their unlabeled forms used to measure J_{HH}, J_{CH}, and J_{CC} values are shown in the Supporting Information. The spectral simulation of 1D ^{1}H NMR spectra using Bruker TopSpin NMR-SIM software[19] gave J_{HH} and J_{CH} values free of second-order effects.

To measure long-range intra-residue $^nJ_{CH}$ values involving the NH hydrogen, two-dimensional (2D) ^{13}C−^{1}H HSQC-HECADE spectra[20] in a 93/7 *v*/*v* $H_2O/^2H_2O$ solvent were recorded with spectral widths of ∼10 and 50−60 ppm for ^{1}H and ^{13}C, respectively, and 16−120 scans per t_1 increment. Data matrices of 4092 (or 8192) × 256 (or 512) points were recorded, and spectra were zero-filled to give final 16384 × 1024 matrices in the ^{1}H and ^{13}C dimensions, respectively. A DIPSI-2 spin-lock was used with a 90-ms mixing time. Scaling factors of 1−10 were applied to avoid spectral crowding by scaling $^1J_{CH}$ values in the indirect dimension. Sign information was obtained from the slopes of the two cross-peak components.

Coupling signs for $^2J_{CH}$ and $^2J_{CC}$ values were determined using empirical projection rules[11,21] and/or are based on signs determined from DFT calculations.

CALCULATION SECTION

Geometry Optimizations. DFT calculations were conducted on fully substituted model structures **6**^{c}−**12**^{c} (Scheme 5) within *Gaussian*16[22] with the B3LYP functional[23,24] and the 6-31G* basis set.[25] In all the geometric optimizations, the effects of solvent water were treated using the self-consistent reaction field (SCRF)[26] and the integral equation formalism polarizable continuum model (IEFPCM).[27] For calculations on **6**^{c}−**11**^{c}, the C1−C2−N2−C1′ torsion angle θ_1 was rotated in 15° increments through 360°, while all other exocyclic torsion angles were either held fixed at 180° (e.g., the C2−N2−C1′−C2′ torsion angle θ_2 in the *N*-acetyl side-chain) or set at initial values and allowed to optimize (for summaries of torsion constraints used in DFT calculations on **6**^{c}−**11**^{c}, see Schemes S2−S7 in the Supporting Information). These calculations yielded 24 geometry-optimized structures for **6**^{c}−**11**^{c} (144 total structures), which were used as an input in *J*-coupling calculations. Similar calculations were conducted on **12** in either its protonated (**12**^{c}p) or ionized (**12**^{c}i) forms, in this case rotating the C4−C5−N5−C1′ torsion angle θ_1 in 15° increments through 360°. The treatment of the exocyclic torsion angles in **12**^{c}p/i during geometry optimization is summarized in Scheme S8 in the Supporting Information.

Calculations of NMR Spin-Coupling Constants. The structural dependencies of 20 J_{HH}, J_{CH}, and J_{CC} values on θ_1 (Scheme 9) were calculated in geometry-optimized structures of **6**^{c}−**12**^{c} using DFT with the B3LYP functional[23,24] in *Gaussian*16.[22] The Fermi contact,[28−30] diamagnetic and paramagnetic spin−orbit, and spin−dipole terms[28] were recovered using a specially designed basis set, [5s^{2}p^{1}d|3s^{1}p],[31] and raw (unscaled) calculated couplings are reported and are accurate to within ±0.2−0.3 Hz based on prior work.[15] The SCRF[26] and the IEFPCM[27] were used to treat the effects of solvent water during the *J*-coupling calculations.

Spin-Coupling Equation Parameterization. Equations relating DFT-calculated J_{HH}, J_{CH}, and J_{CC} values to θ_1 in **6**^{c}−**12**^{c} were parameterized using *R*. Equations were parameterized using *J*-values calculated in a sub-population of conformers that was selected using a 10 kcal/mol energy cutoff to remove highly strained conformers.[10] A secondary constraint was also applied when needed to remove DFT-optimized structures containing distorted aldohexopyranosyl rings; Cremer−Pople puckering parameters were calculated from DFT-generated

https://doi.org/10.1021/acs.joc.2c00189
J. Org. Chem. 2022, 87, 8368−8379

Scheme 9. Twenty Spin-Coupling Constants in 6^c−11^c Whose Dependencies on θ_1 were Calculated, Illustrated for 7^c

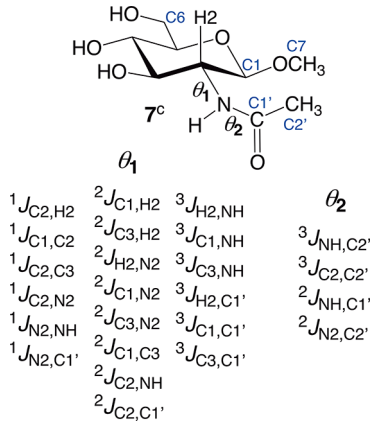

Cartesian coordinates and a θ value of 35° was used as the cutoff.[10] The plots of calculated J-couplings in structures 6^c−12^c as a function of θ_1 were parameterized and are found in the Supporting Information (eqs S1−S60). The curves were fitted to the following modified Karplus-like equation (eq 1) using R.

$$^{n}J_{X,Y}\ (\mathrm{Hz}) = k + a\cos\theta_1 + b\sin\theta_1 + c\cos 2\theta_1 + d\sin 2\theta_1 + e\cos 3\theta_1 + f\sin 3\theta_1 \quad (1)$$

This generalized form of the Karplus-like equation was first described by Pachler.[32] This trigonometric function accounts for asymmetry in the Karplus curve caused by the substitution of a hydrogen atom in the coupling pathway. This form was adopted in this work because it provides the best parameterization of the DFT data with the smallest number of terms. This form is also amenable to simple integration, making it compatible with *MA'AT* analysis[10] for modeling torsional populations in a solution. The goodness-of-fit of each equation is reported as an RMSD. Equation parameterization was also evaluated using the Akaike information criterion,[33] resulting in truncated forms of some equations.

Brief Description of the *MA'AT* Method. The relationship between molecular torsion angles and NMR spin-couplings is well established,[34,35] which allows theoretical methods to produce a function $J(\theta)$ that describes this dependence. NMR observables are averaged over the entire population and do not yield conformations of single molecules. Therefore, the experimental J-coupling (J_{exp}) can be quantified using eq 2, where $J(\theta)$ is the function describing the torsional dependence of the J-coupling and $\rho(\theta)$ is the population density.

$$J_{exp} = \int_0^{2\pi} J(\theta)\rho(\theta)\,\mathrm{d}\theta \quad (2)$$

The *MA'AT* method to determine rotamer population distributions evaluates eq 2 directly. The method uses a trigonometric polynomial to represent $J(\theta)$ (eq 1) and either a wrapped normal or von Mises distribution to represent $\rho(\theta)$. The method then uses an ensemble of redundant NMR J-couplings that depend on the same torsion angle to solve for optimal values of the population model. This result is achieved by calculating spin-coupling constants for the ensemble from population distributions generated from a Monte Carlo simulation. The calculated J-couplings are compared to the experimental values to give a RMSD for each population model. The models that give the lowest RMSD are further optimized using the Nelder−Mead derivative-free algorithm.[36,37] A web-based application with the same name as the method has been encoded in R as a Shiny application and is available at https://rmeredit.shinyapps.io/maat24/.

Aqueous MD Simulations. Initial structures of 6^c, 7^c, 10^c, and 13^c were built using the carbohydrate builder module available on the GLYCAM website (http://www.glycam.org).[38] The GLYCAM06[39] (version j) force field was employed in all the simulations. Structures 6^c, 7^c, 10^c, and 13^c were solvated with TIP3P[40] water using a 12 Å buffer in a cubic box, using the LEaP module in the AMBER 14 software package.[41] Energy minimizations for solvated 6^c, 7^c, 10^c, and 13^c were performed separately under constant volume (500 step steepest descent, followed by 24,500 steps of conjugate gradient minimization). Each system was subsequently heated to 300 K over a period of 50 ps, followed by equilibration at 300 K for a further 0.5 ns using the *nPT* condition, with the Berendsen thermostat[42] for temperature control. All covalent bonds involving hydrogen atoms were constrained using the SHAKE algorithm,[43] allowing a simulation time step of 2 fs throughout the simulation. After equilibration, production simulations were carried out with the GPU (graphics processing unit) implementation[44] of the PMEMD.MPI module, and trajectory frames were collected every 1 ps for a total of 1 μs. One to four nonbonded interactions were not scaled[45] and a nonbonded cutoff of 8 Å was applied to van der Waals interactions, with long-range electrostatics treated with the particle mesh Ewald approximation. The output from each MD simulation was imported into *Prism*[46] for visualization.

■ ASSOCIATED CONTENT

Supporting Information

The Supporting Information is available free of charge at https://pubs.acs.org/doi/10.1021/acs.joc.2c00189.

Spin-coupling constants in *N*-acetyl side-chains of saccharides and analogous spin-couplings in peptides and proteins; torsion angle constraints used in DFT calculations of 6^c−12^c; parameterized equations for θ_1 in 6^c−12^c; dependencies of calculated J-couplings on θ_1 in 6^c−12^c; synthesis and NMR spectra of $6^{1'}$ and $7^{1'}$; synthesis, NMR, and mass spectrometry (MS) spectra of $10^{1'}$; spin-coupling ensembles used in the *MA'AT* modeling of θ_1 in **6**, **7**, and **10** in aqueous solution and DMSO-d_6; *MA'AT* analysis of θ_1 in **6**, **7**, and **10**—modeling results and statistics in aqueous solution and DMSO-d_6; *MA'AT* models of θ_1 in **6**, **7**, and **10** using J-couplings measured in aqueous solutions and DMSO-d_6; statistical data on *N*-acetylated sugar side-chain conformations taken from the PDB; percentages of *cis* and *trans* amide configurations in *N*-acetylated sugars in the PDB; histograms showing the distribution of θ_1 and θ_2 in *N*-acetylated sugar residues in crystal structures deposited in the PDB; synthesis, NMR and MS data for $13^{1''1'''}$; spin-coupling ensembles used in *MA'AT* modeling of θ_1 in **13** in aqueous solution and DMSO-d_6; *MA'AT* analysis of θ_1 in **13**, showing modeling results and statistics in aqueous solution and DMSO-d_6; *MA'AT* models of θ_1 and θ_1' in **13** using J-couplings measured in aqueous solution and DMSO-d_6; representative param-

https://doi.org/10.1021/acs.joc.2c00189
J. Org. Chem. 2022, 87, 8368−8379

eter space plots from *MA'AT* fits of θ_1 in **6**, **7**, **10**, and **13**; representative NMR spectra of unlabeled and ^{13}C-labeled **6**, **7**, **10**, and **13** for measurements of θ_1-sensitive spin-coupling constants; and Cartesian coordinates for representative structures **6**^{c}−**12**^{c} (PDF)

AUTHOR INFORMATION

Corresponding Author

Anthony S. Serianni − *Department of Chemistry and Biochemistry, University of Notre Dame, Notre Dame, Indiana 46556-5670, United States;* orcid.org/0000-0001-6114-1446; Email: aseriann@nd.edu

Authors

Reagan J. Meredith − *Department of Chemistry and Biochemistry, University of Notre Dame, Notre Dame, Indiana 46556-5670, United States*

Timothy Tetrault − *Department of Chemistry and Biochemistry, University of Notre Dame, Notre Dame, Indiana 46556-5670, United States*

Mi-Kyung Yoon − *Department of Chemistry and Biochemistry, University of Notre Dame, Notre Dame, Indiana 46556-5670, United States*

Wenhui Zhang − *Department of Chemistry and Biochemistry, University of Notre Dame, Notre Dame, Indiana 46556-5670, United States*

Ian Carmichael − *Radiation Laboratory, University of Notre Dame, Notre Dame, Indiana 46556-5670, United States*

Complete contact information is available at: https://pubs.acs.org/10.1021/acs.joc.2c00189

Notes

The authors declare no competing financial interest.

ACKNOWLEDGMENTS

This work was supported by the National Science Foundation (CHE 1707660 and CHE 2002625 to A.S.) and by Omicron Biochemicals, Inc., South Bend, IN. The Notre Dame Radiation Laboratory is supported by the Department of Energy Office of Science, Office of Basic Energy Sciences, under award number DE-FC02-04ER15533. This is document number NDRL 5324.

REFERENCES

(1) Yu, H.; Chen, X. Carbohydrate Post-glycosylational Modifications. *Org. Biomol. Chem.* **2007**, *5*, 865−872.

(2) Eberharter, A.; Becker, P. B. Histone Acetylation: A Switch Between Repressive and Permissive Chromatin. *EMBO Rep.* **2002**, *3*, 224−229.

(3) De Oliveira, J. R.; Rosa, J. L.; Ambrosio, S.; Bartrons, R. Effect of Galactosamine on Hepatic Carbohydrate Metabolism: Protective Role of Fructose 1,6-Bisphosphate. *Hepatology* **1992**, *15*, 1147−1153.

(4) Hu, X.; Zhang, W.; Carmichael, I.; Serianni, A. S. Amide *Cis-Trans* Isomerization in Aqueous Solutions of Methyl *N*-Formyl-D-glucosaminides and Methyl *N*-Acetyl-D-Glucosaminides: Chemical Equilibria and Exchange Kinetics. *J. Am. Chem. Soc.* **2010**, *132*, 4641−4652.

(5) Turney, T.; Pan, Q.; Sernau, L.; Carmichael, I.; Zhang, W.; Wang, X.; Woods, R. J.; Serianni, A. S. *O*-Acetyl Side-Chains in Monosaccharides: Redundant NMR Spin-Couplings and Statistical Models for Acetate Ester Conformational Analysis. *J. Phys. Chem. B* **2017**, *121*, 66−77.

(6) Holmbeck, S. M. A.; Petillo, P. A.; Lerner, L. E. The Solution Conformation of Hyaluronan: A Combined NMR and Molecular Dynamics Study. *Biochemistry* **1994**, *33*, 14246−14255.

(7) Mobli, M.; Almond, A. *N*-Acetylated Amino Sugars: The Dependence of NMR $^3J_{(HN,H2)}$ Couplings on Conformation, Dynamics and Solvent. *Org. Biomol. Chem.* **2007**, *5*, 2243−2251.

(8) Zhu, Y.; Pan, Q.; Thibaudeau, C.; Zhao, S.; Carmichael, I.; Serianni, A. S. [^{13}C,^{15}N]2-Acetamido-2-deoxy-D-aldohexoses and Their Methyl Glycosides: Synthesis and NMR Investigations of *J*-Couplings Involving ^{1}H, ^{13}C and ^{15}N. *J. Org. Chem.* **2006**, *71*, 466−479.

(9) Hu, X.; Carmichael, I.; Serianni, A. S. *N*-Acetyl Side-Chains in Saccharides: NMR *J*-Coupling Equations Sensitive to CH−NH and NH−CO Bond Conformations in 2-Acetamido-2-deoxy-aldohexopyranosyl Rings. *J. Org. Chem.* **2010**, *75*, 4899−4910.

(10) Zhang, W.; Turney, T.; Meredith, R.; Pan, Q.; Sernau, L.; Wang, X.; Hu, X.; Woods, R. J.; Carmichael, I.; Serianni, A. S. Conformational Populations of β-(1→4) *O*-Glycosidic Linkages Using Redundant NMR *J*-Couplings and Circular Statistics. *J. Phys. Chem. B* **2017**, *121*, 3042−3058.

(11) Bock, K.; Pedersen, C.; Popoff, T.; Theander, O.; Nørskov, L.; Schroll, G. Two- and Three-Bond ^{13}C-^{1}H Couplings in Some Carbohydrates. *Acta Chem. Scand. Ser. B* **1977**, *31*, 354−358.

(12) Bose-Basu, B.; Klepach, T.; Bondo, G.; Bondo, P. B.; Zhang, W.; Carmichael, I.; Serianni, A. S. ^{13}C-^{13}C NMR Spin-Spin Coupling Constants in Saccharides: Structural Correlations Involving All Carbons In Aldopyranosyl Rings. *J. Org. Chem.* **2007**, *72*, 7511−7522.

(13) Hadad, M. J.; Zhang, W.; Turney, T.; Sernau, L.; Wang, W.; Woods, R. J.; Incandela, A.; Surjancev, I.; Wang, A.; Yoon, M.-K.; Coscia, A.; Euell, C.; Meredith, R.; Carmichael, I.; Serianni, A. S. NMR Spin-Couplings in Saccharides: Relationships Between Structure, Conformation and the Magnitudes of J_{HH}, J_{CH} and J_{CC} Values. In *New Developments in NMR 10: NMR in Glycoscience and Glycotechnology*; Peters, T., Kato, K., Eds.; Royal Society of Chemistry, 2017; pp 20−100.

(14) Serianni, A. S.; Bondo, P. B.; Zajicek, J. Verification of the Projection Resultant Method for Two-Bond ^{13}C-^{13}C Coupling Sign Determinations in Carbohydrates. *J. Magn. Reson. Ser. B* **1996**, *112*, 69−74.

(15) Podlasek, C. A.; Wu, J.; Stripe, W. A.; Bondo, P. B.; Serianni, A. S. [^{13}C]Enriched Methyl Aldopyranosides: Structural Interpretations of ^{13}C-^{1}H Spin-Coupling Constants and ^{1}H Chemical Shifts. *J. Am. Chem. Soc.* **1995**, *117*, 8635−8644.

(16) Lepsik, M.; Sommer, R.; Kuhaudomlarp, S.; Lelimousin, M.; Paci, E.; Varrot, A.; Titz, A.; Imberty, A. Induction of a Rare Conformation of Oligosaccharide by Binding to a Calcium-Dependent Bacterial Lectin: A X-ray Crystallography and Modelling Study. *Eur. J. Med. Chem.* **2019**, *177*, 212−220.

(17) Pluth, M. D.; Bergman, R. G.; Raymond, K. N. Acceleration of Amide Bond Rotation by Encapsulation in the Hydrophobic Interior of a Water-Soluble Supramolecular Assembly. *J. Org. Chem.* **2008**, *73*, 7132−7136.

(18) Wiberg, K. B.; Rablen, P. R.; Rush, D. J.; Keith, T. A. Amides. 3. Experimental and Theoretical Studies of the Effect of the Medium on the Rotational Barriers for *N*,*N*-Dimethylformamide and *N*,*N*-Dimethylacetamide. *J. Am. Chem. Soc.* **1995**, *117*, 4261−4270.

(19) TopSpin Users Guide: NMR-SIM; Bruker: Massachusetts, 2021. https://www.bruker.com/en.html (last accessed March 29, 2022).

(20) Koźmiński, W.; Nanz, D. Sensitivity Improvement and New Acquisition Scheme of Heteronuclear Active-Coupling-Pattern-Tilting Spectroscopy. *J. Magn. Reson.* **2000**, *142*, 294−299.

(21) Church, T.; Carmichael, I.; Serianni, A. S. Two-bond ^{13}C-^{13}C Spin-coupling Constants in Carbohydrates: Effect of Structure on Coupling Magnitude and Sign. *Carbohydr. Res.* **1996**, *280*, 177−186.

(22) Frisch, M. J.; Trucks, G. W.; Schlegel, H. B.; Scuseria, G. E.; Robb, M. A.; Cheeseman, J. R.; Scalmani, G.; Barone, V.; Petersson, G. A.; Nakatsuji, H.; Li, X.; Caricato, M.; Marenich, A. V.; Bloino, J.; Janesko, B. G.; Gomperts, R.; Mennucci, B.; Hratchian, H. P.; Ortiz, J.

V.; Izmaylov, A. F.; Sonnenberg, J. L.; Williams-Young, D.; Ding, F.; Lipparini, F.; Egidi, F.; Goings, J.; Peng, B.; Petrone, A.; Henderson, T.; Ranasinghe, D.; Zakrzewski, V. G.; Gao, J.; Rega, N.; Zheng, G.; Liang, W.; Hada, M.; Ehara, M.; Toyota, K.; Fukuda, R.; Hasegawa, J.; Ishida, M.; Nakajima, T.; Honda, Y.; Kitao, O.; Nakai, H.; Vreven, T.; Throssell, K.; Montgomery, J. A., Jr.; Peralta, J. E.; Ogliaro, F.; Bearpark, M. J.; Heyd, J. J.; Brothers, E. N.; Kudin, K. N.; Staroverov, V. N.; Keith, T. A.; Kobayashi, R.; Normand, J.; Raghavachari, K.; Rendell, A. P.; Burant, J. C.; Iyengar, S. S.; Tomasi, J.; Cossi, M.; Millam, J. M.; Klene, M.; Adamo, C.; Cammi, R.; Ochterski, J. W.; Martin, R. L.; Morokuma, K.; Farkas, O.; Foresman, J. B.; Fox, D. J. *Gaussian 16*, Revision B.01; Gaussian, Inc.: Wallingford, CT, 2016.

(23) Becke, A. D. Density-Functional Thermochemistry. III. The Role of Exact Exchange. *J. Chem. Phys.* **1993**, *98*, 5648−5652.

(24) Becke, A. D. A New Mixing of Hartree-Fock and Local Density-Functional Theories. *J. Chem. Phys.* **1993**, *98*, 1372−1377.

(25) Hehre, W. J.; Ditchfield, R.; Pople, J. A. Self-Consistent Molecular Orbital Methods. XII. Further Extensions of Gaussian-Type Basis Sets for Use in Molecular Orbital Studies of Organic Molecules. *J. Chem. Phys.* **1972**, *56*, 2257−2261.

(26) Cancès, E.; Mennucci, B.; Tomasi, J. A New Integral Equation Formalism for the Polarizable Continuum Model: Theoretical Background and Applications To Isotropic and Anisotropic Dielectrics. *J. Chem. Phys.* **1997**, *107*, 3032−3041.

(27) Cammi, R.; Mennucci, B.; Tomasi, J. Fast Evaluation of Geometries and Properties of Excited Molecules in Solution: A Tamm-Dancoff Model with Application to 4-Dimethyl-amino-benzonitrile. *J. Phys. Chem. A* **2000**, *104*, 5631−5637.

(28) Sychrovský, V.; Gräfenstein, J.; Cremer, D. Nuclear Magnetic Resonance Spin-Spin Coupling Constants from Coupled Perturbed Density Functional Theory. *J. Phys. Chem. A* **2000**, *113*, 3530−3547.

(29) Helgaker, T.; Watson, M.; Handy, N. C. Analytical Calculation of Nuclear Magnetic Resonance Indirect Spin-Spin Coupling Constants at the Generalized Gradient Approximation and Hybrid Levels of Density-Functional Theory. *J. Chem. Phys.* **2000**, *113*, 9402−9409.

(30) Barone, V.; Peralta, J. E.; Contreras, R. H.; Snyder, J. P. DFT Calculation of NMR J_{FF} Spin-Spin Coupling Constants in Fluorinated Pyridines. *J. Phys. Chem. A* **2002**, *106*, 5607−5612.

(31) Klepach, T.; Zhao, H.; Hu, X.; Zhang, W.; Stenutz, R.; Hadad, M. J.; Carmichael, I.; Serianni, A. S. Informing Saccharide Structural NMR Studies with Density Functional Theory Calculations. In *Glycoinformatics: Methods in Molecular Biology*; Lütteke, T., Frank, M., Eds.; Springer: New York, 2015; pp 289−331.

(32) Pachler, K. G. R. Extended Hückel Theory MO Calculations of Proton-Proton Coupling Constants−II: The Effect of Substituents on Vicinal Couplings in Monosubstituted Ethanes. *Tetrahedron* **1971**, *27*, 187−199.

(33) Akaike, H. A New Look at the Statistical Model Identification. *IEEE Trans. Autom. Control* **1974**, *19*, 716−723.

(34) Karplus, M. Contact Electron-Spin Coupling Nuclear Magnetic Moments. *J. Chem. Phys.* **1959**, *30*, 11−15.

(35) Karplus, M. Vicinal Proton Coupling in Nuclear Magnetic Resonance. *J. Am. Chem. Soc.* **1963**, *85*, 2870−2871.

(36) Nelder, J. A.; Mead, R. A Simplex Method for Function Minimization. *Comput. J.* **1965**, *7*, 308.

(37) Varadhan, R.; Borchers, H. W. ABB Corporate Research R Package, 2016. https://CRAN.R-project.org/package=dfoptim (last accessed March 29, 2002).

(38) Complex Carbohydrate Research Center (CRCC); University of Georgia. http://www.glycam.org (last accessed March 29, 2022).

(39) Kirschner, K. N.; Yongye, A. B.; Tschampel, S. M.; González-Outeiriño, J.; Daniels, C. R.; Foley, B. L.; Woods, R. J. GLYCAM06: A Generalizable Biomolecular Force Field. Carbohydrates. *J. Comput. Chem.* **2008**, *29*, 622−655.

(40) Jorgensen, W. L.; Chandrasekhar, J.; Madura, J. D.; Impey, R. W.; Klein, M. L. Comparison of Simple Potential Functions for Simulating Liquid Water. *J. Chem. Phys.* **1983**, *79*, 926−935.

(41) Case, D. A.; Babin, V.; Berryman, J. T.; Betz, R. M.; Cai, Q.; Cerutti, D. S.; Cheatham, T. E. I.; Darden, T. A.; Duke, R. E.; Gohlke, H.; Goetz, A. W.; Gusarov, S.; Homeyer, N.; Janowski, P.; Kaus, J.; Kolossváry, I.; Kovalenko, A.; Lee, T. S.; LeGrand, S.; Luchko, T.; Luo, R.; Madej, B.; Merz, K. M.; Paesani, F.; Roe, D. R.; Roitberg, A.; Sagui, C.; Salomon-Ferrer, R.; Seabra, G.; Simmerling, C. L.; Smith, W.; Swails, J.; Walker, R. C.; Wang, J.; Wolf, R. M.; Wu, X.; Kollman, P. A. *AMBER 14*; University of California: San Francisco, 2014.

(42) Berendsen, H. J. C.; Postma, J. P. M.; van Gunsteren, W. F.; DiNola, A.; Haak, J. R. Molecular Dynamics With Coupling to an External Bath. *J. Chem. Phys.* **1984**, *81*, 3684−3690.

(43) van Gunsteren, W. F.; Berendsen, H. J. C. Algorithms for Macromolecular Dynamics and Constraint Dynamics. *Mol. Phys.* **1977**, *34*, 1311−1327.

(44) Götz, A. W.; Williamson, M. J.; Xu, D.; Poole, D.; Le Grand, S.; Walker, R. C. Routine Microsecond Molecular Dynamics Simulations with AMBER on GPUs. 1. Generalized Born. *J. Chem. Theory Comput.* **2012**, *8*, 1542−1555.

(45) Kirschner, K. N.; Woods, R. J. Solvent Interactions Determine Carbohydrate Conformation. *Proc. Natl. Acad. Sci. USA.* **2001**, *98*, 10541−10545.

(46) *Prism 8 for Mac OS X*, ver 8.4.2 (464); GraphPad Software, 2020.

https://doi.org/10.1021/acs.joc.2c00189
J. Org. Chem. 2022, 87, 8368−8379